JOURNAL OF SPACECRAFT AND ROCKETS
Vol. 37, No. 2, March–April 2000

Aerothermodynamic Performance Enhancement of Sphere-Cones Using the Artificially Blunted Leading-Edge Concept

Anurag Gupta* and Stephen M. Ruffin†
Georgia Institute of Technology, Atlanta, Georgia 30332-0150
Mark E. Newfield‡
NASA Ames Research Center, Moffett Field, California 94035-1000
and
Leslie Yates§
Aerospace Computing, Inc., Los Altos, California 94022

Artificially blunted leading edges created by the use of a flow-through channel sized to choke at supersonic conditions have been shown to be effective in significantly reducing drag in high-speed flow over blunted airfoils. Results of the work to apply the concept to blunted sphere-cones and the use of a channel at a leading edge to enhance lift are presented. This enhancement is caused by the internal flow creating suction at the channel lip. Proof-of-concept numerical simulations on various sphere-cone configurations at different flight conditions show the concept's effectiveness in reducing drag of axisymmetric bodies. Experimental data are used to validate the predicted drag reduction at $\alpha = 0$ deg, Mach 2.25–2.5 range, and sea-level conditions. Direct correlations between the channel size and drag reduction, lip geometry and lift increment, as well as between the channel lip radius and peak heat-transfer rates, were established and characterized using an efficient concept evaluation method. These polynomial models for force coefficients and heat-transfer rates are used by a gradient-based optimizer to generate derivatives of a 10-deg sphere-cone with the concept for operation at Mach 7, 20 km altitude. These geometries had approximately 5% higher lift-to-drag ratio and similar peak heating rates as the baseline. To mitigate the potential system-level drawbacks caused by a straight channel, a cowl-like derivative with curved channels exhausting from the forebody was investigated and found to provide comparable performance enhancement.

Nomenclature

c = chord length, m
c_d = coefficient of drag, with reference area $= (\pi d_b^2/4)$
c_l = coefficient of lift, with reference area $= (\pi d_b^2/4)$
d_b = base diameter, m
h = altitude, km
M_n = Mach number normal to leading edge
M_∞ = freestream Mach number
q_∞ = freestream dynamic pressure, Pa
r_c = channel radius, m
r_n = nose radius, m
$r_{n,l}$ = radius of the lip at the channel entrance, m
T_{wall} = temperature of isothermal wall, K
α = angle of attack, deg

Introduction

THE lift-to-drag ratio (L/D) of supersonic and hypersonic vehicles like planetary entry vehicles, missiles, launch vehicles, etc., has a strong impact on performance criteria like cross range, maneuver requirements, and payload mass fractions and on their economic viability. Much of the drag on supersonic and hypersonic vehicles is caused by zero-lift bluntness drag. This component of drag (the wave drag caused by the vehicle's thickness and bluntness of the leading and trailing edges in a zero-lift orientation) increases rapidly with freestream Mach number and can be responsible for well over 33% of the total vehicle drag when the leading edge is supersonic. As aerothermal, manufacturing, structural, and low-speed aerodynamic issues force the leading edges of high-speed vehicles to be blunted, drag reduction via reduction of the zero-lift bluntness drag promises to be very effective.

The present concept allows for a channel to be opened at supersonic/hypersonic cruise in the vehicle's nose or airfoil sections that make up the wings or other appendages. The channel begins at the leading edge of the body with freestream air flowing passively through the channel. With the $M_n > 1$ at the nose/leading edge of a no-channel blunted body, the surface pressure in the stagnation region is high and responsible for much of the wave drag. With the channel opened, the vehicle surface that experienced most of the high, near-stagnation pressure is removed, leading to lower wave drag. An effective blunt-body flow structure is possible when the channel is sized so that a choked flow condition exists (see Fig. 1) at a specified range of flight Mach numbers. A normal shock rests in front of the channel entrance, and the flow enters the channel subsonically. Thus an artificially blunted leading edge (ABLE) is created. In previous seminal work Ruffin and Gupta[1] conducted a preliminary investigation of the drag-reduction concept applied to a blunted diamond airfoil. The concept was shown to be effective, and the ABLE flow structure shown to be robust to changes in angle of attack and flight conditions as long as M_n was supersonic. The aerodynamic performance of airfoils employing the ABLE concept was measured over a range of channel geometries, angles of attack, and flight conditions. The ABLE airfoils had their total drag reduced by over 30 and 20% (for laminar and turbulent flow) relative to geometries without channels because of a much lower wave drag and slightly increased skin-friction drag. However, maximum heat-transfer rates, which depended on the radii of the channel entrance lips, were found to impose limits on the effectiveness of this concept.

To evaluate the possibility of designing an ABLE airfoil that would reduce drag without paying any penalties in other areas like lifting capacity, maximum heating rates or enclosed volume, an aerothermodynamic design methodology was formulated and executed by Gupta and Ruffin.[2] The methodology used multidisciplinary design optimization (MDO) techniques like design of

Received 18 March 1999; revision received 8 December 1999; accepted for publication 12 December 1999.

*Ph.D. Candidate, Student Member AIAA.
†Associate Professor, School of Aerospace Engineering. Associate Member AIAA.
‡Research Scientist, Space Technology Division. Member AIAA.
§Vice President. Senior Member AIAA.

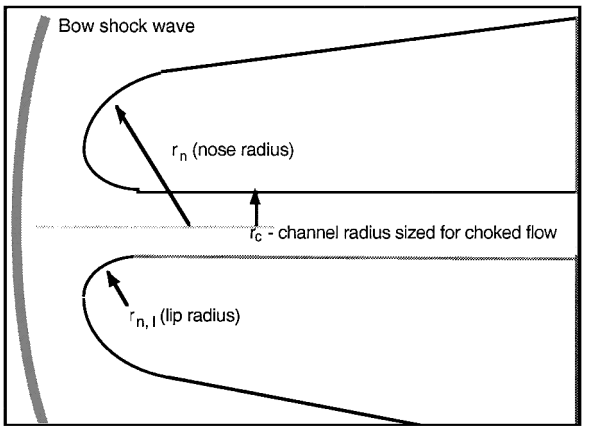

Fig. 1 Flow structure with choked channel creating the ABLE geometry.

experiments and response surface methods (RSM) in conjunction with high-fidelity Reynolds-averaged Navier–Stokes (RANS) solutions to characterize the design space for ABLE airfoils derived from a blunted diamond airfoil operating at $\alpha = 4$ deg, Mach 4 and 12 km altitude. The optimal airfoil obtained using a gradient-based optimizer operating on five geometric design variables showed a drag reduction of about 19%, a lower maximum heat-transfer rate, while matching the c_l and enclosed area (to meet structural/packaging requirements).

The configurations, and hence the lifting efficiencies and maneuverability of blunted high-speed vehicles like reentry vehicles, missile warheads, etc., are often restrained by aerothermal and packaging constraints. While testing the applicability of the channel-in-vehicle concept to three dimensional flowfields, it was noticed that the flow expanding over the channel lip creates a suction region that significantly increases lift relative to a conventional body. Thus, applying the ABLE concept to blunted nonslender geometries could increase L/D by decreasing drag *and* increasing lift. An added advantage lies in its potential for providing variable L/D, i.e., a vehicle could find it advantageous to have high drag in the initial stages of atmospheric entry (channel closed off) and then open the channel to obtain high L/D for better cross range, maneuverability, or trajectory control. This paper describes research with twin goals: to verify and understand these mechanisms of increasing L/D and to use a previously tested method[2] for an aerothermodynamic design of an ABLE sphere-cone. A sphere-cone geometry was chosen because it is representative of a widely used geometry for reentry vehicles and hypersonic vehicle forebodies.

Analysis Techniques

Flow Solver

Predictions of aerodynamic and thermal loads are obtained using GASP.[3] This computer code is a well-validated, multizone, finite volume code that solves the unsteady, three-dimensional, RANS equations and its subsets. All of the simulations assumed the air to be a perfect gas. Calculations assuming laminar and fully turbulent flow were conducted. In the latter case, the algebraic Baldwin–Lomax model was used with turbulent flow modeled as beginning at the leading edge. A constant T_{wall} boundary condition was used at all vehicle surfaces except in the base region, where an adiabatic wall boundary condition was used. The external and internal channel flows were computed in a fully coupled manner.

Inviscid flux terms were evaluated using third-order, upwind-biased, Van Leer flux vector splitting, and the viscous cross-derivative terms were evaluated only in the streamwise planes. For higher-order spatial accuracy MUSCL interpolation in conjunction with the minmod limiter was used for the initial cases; for the design study simulations the essentially nonoscillatory scheme was used to avoid the characteristic leveling off and oscillation of residuals with the minmod limiter. Two types of implicit time-integration strategies were used: two-factor approximate factorization/hybrid relaxation with sweeping in the circumferential direction for the initial cases, and Jacobi time integration with inner iterations for the design cases.

Grid Generation

The GRIDGEN[4] software was used to create 1) axisymmetric grids for the initial $\alpha = 0$ deg cases and 2) three-dimensional grids over half of the sphere-cone for the lifting ($\alpha \neq 0$ deg) cases. The axisymmetric grids were relatively coarse (13,600 nodes per plane) with the forebody zone having 53 body-normal grid points and 90 points in the streamwise direction. A study of the effectiveness of different grid topologies in maintaining off-the-wall spacing without destroying orthogonality to the body walls was conducted. The variation in near-wall grid spacing with choice of topology was significant and affected the prediction of maximum heat-transfer rates. The best topology for heat transfer, depicted in Fig. 2, had the body-parallel family of grid lines turning across the bow-shock wave and was adopted for the three-dimensional grids. Based on earlier experience and the need to balance sufficient accuracy with grid size for the design study, the forebody zone had approximately 50 points in the body-normal direction, 37 points in the circumferential direction, and 133 points in the streamwise direction. At least 15 points were placed inside the boundary layer, and the channel was spanned by 33–37 points depending on the channel radius with care taken to ensure that the near wall grid remains the same. The outer boundary was placed within 5–10 points off the bow shock. As the predicted heating rate is most sensitive to the grid spacing normal to the wall, a grid-refinement study was also carried out to verify the validity of choice of grid dimensions normal to the wall. Fine grids were created with twice the number of points in the direction normal to the wall by inserting grid nodes between every pair of nodes in the original grid. GASP solutions with the same input parameters on these fine grids showed that c_l and c_d values using the finer grid were off by $+1.31$ and -0.61%, respectively, primarily because of better resolution in the base flow region. Thus, we estimate that the calculated lift and drag results presented are within an acceptable 1.5% of those obtained from the fine grid solutions. Researchers using GASP[5] for similar aerothermal calculations have found that the wall heating rate values were fairly grid independent for cell heights of $\mathcal{O}(1 \times 10^{-06}$ m). For our grids the first grid point of the wall was placed at 1×10^{-06} m, with the cell Reynolds numbers (based on local sonic speed) ranging from 6 to 30. The use of the elliptic solver in GRIDGEN and variations in actual geometry create small variations in off-the-wall spacing that introduce noise in the eventual responses, i.e., force coefficients and heat-transfer rates. The latter, being local quantities rather than obtained by integration over the entire geometry, are especially sensitive to variations in grid spacing and skewness. To capture the relative variations in thermal loading because of geometry and flowfield changes accurately, a consistent off-the-wall grid spacing was used. The centerline heat-transfer-rate distributions

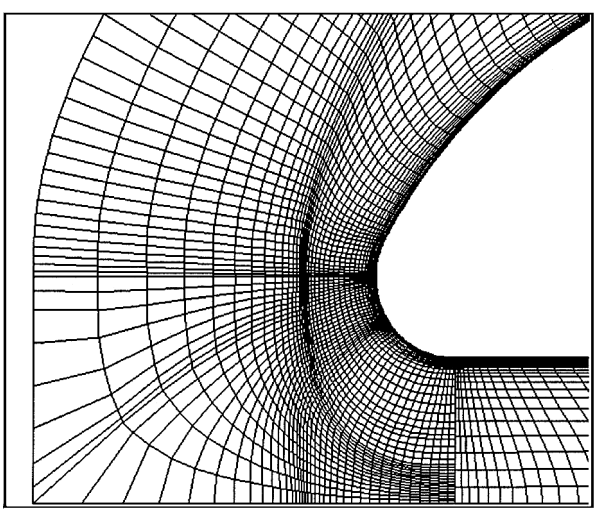

Fig. 2 Topology chosen for nose region grids.

were tracked and convergence declared when these profiles stopped varying.

Convergence Acceleration

To improve the speed of the solution process, the mesh-sequencing feature of GASP was used. Each block was typically coarsened by a factor of two twice to create the medium and coarse grids. The solution was converged by 2–3 orders of magnitude on each level to obtain the final inviscid solution. The order of flux reconstruction was also lowered for the solutions over coarse grids. With the main flow features defined and especially to mitigate the nonalignment of grid lines with the bow shock near the axis of the body, the grids were adapted to the flow before computing the viscous solution. This was done using the Self-Adaptive Grid Code,[6] a multidimensional self-adaptive grid code that redistributes grid points to the strong gradient regions. However, this code adapts the grid as a sequence of one-dimensional adaptations and in some cases skews the grids. As a result, some grids had to be adapted by going back to the grid generator to redistribute points.

Proof-of-Concept Results

In this section results for initial investigations of ABLE sphere-cone geometries are presented. Two different baseline (sphere-cones without channels) geometries and their ABLE derivatives were tested at different conditions.

Ten-Degree Sphere-Cone at Mach 7 Lifting Conditions

The first set of numerical results is for axisymmetric flow around 10-deg sphere-cones at Mach 7, 20 km altitude. The baseline geometry was a 10-deg sphere-cone with a nose radius of 0.35 m, a base diameter of 1 m, length of 1.164 m, and is shown in Fig. 3. Figure 4 depicts the ABLE geometry derived from this baseline by coring out a channel of radius 0.09 m and rounding off the channel lips to a radius of 0.05 m. The results presented first are lifting calculations at $\alpha = 5$ deg using the high-resolution grids.

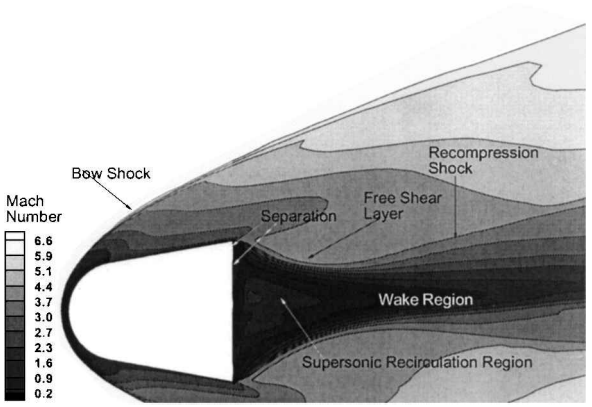

Fig. 3 Schematic and Mach-number distribution for blunted sphere-cone flowfield: $M_\infty = 7$, $h = 20$ km, and $\alpha = 5$ deg.

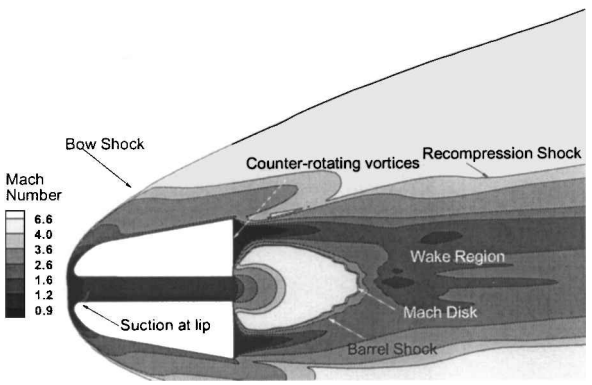

Fig. 4 Schematic and Mach-number distribution for ABLE sphere-cone ($r_c = 0.09$ m, $r_{nose} = 0.05$ m) flowfield: $M_\infty = 7.0$, $h = 20$ km, and $\alpha = 5$ deg.

Figure 3 is a schematic of the blunt-body flowfield overlaid over a Mach-number distribution picture. The flow goes through the (normal) bow shock at the nose and expands around the sphere-cone shoulder quickly becoming supersonic. As the boundary layer develops over the cone, it separates to form a free shear layer as the flow expands around the base corner. The free shear layer necks down into the wake region and then turns back into the freestream direction, giving rise to a recompression oblique shock. An analysis of computed velocity vectors reveals a pair of counter-rotating recirculation vortices formed in the base region with the relative size and strength of each depending on the symmetry of the flowfield. For $\alpha = 5$ deg the lower vortex is slightly smaller. The recirculation is strong enough for the velocities to go supersonic and is therefore slowed down by an embedded normal shock near the base. This normal shock increases the pressure acting on the base and lowers drag relative to a sphere-cone geometry without such a shock.

Figure 4 presents a similar Mach-number distribution for the ABLE body flowfield. Note the similarities in external flow structure with the baseline geometry. The channel is choked, forming the effective blunt leading edge as predicted. At angle of attack the flow at the channel entrance is nonsymmetric. As the subsonic flow expands over the lower lip, it accelerates and creates a suction peak above the lower channel wall. In effect, while the overall flow still sees the effective blunt body, the flow near the nosetip, after being slowed to subsonic speeds by the normal shock, sees a more slender nose to expand over and creates a suction region. For the geometries considered here, the flow expanded to supersonic speeds, and the expansion fan ricochets between the channel walls making the flow nearly symmetric shortly downstream of the entrance region. The internal flow is like a high-pressure underexpanded jet and exhausts creating flow structures similar to jet plumes. The size of the plume region depends on how underexpanded the flow in the channel is. As is characteristic of severely underexpanded flows typically seen in propulsive flowfields, a barrel shock structure ending in a Mach disc forms and is clearly visible as shown in Fig. 4. Also, the presence of two sharply expanding flows severely curtails the size of the recirculation regions at the base even though the flow structure is similar with two counter-rotating vortices. As all of the cases were at 0 deg yaw, the maximum heating occurs in the plane of symmetry.

Table 1 presents a comparison of the force coefficients (based on the baseline base area) and peak heat-transfer rates for the two configurations. Although the drag reduction was only about 3.56%, the suction at the lip increased c_l by 20.6% and hence increased the L/D ratio by 25.1%. The drag breakdowns for each geometry are compared in Fig. 5. ABLE provides a forebody inviscid drag reduction of 5.4% while slightly increasing the viscous drag and base drag. The small lip radius of 0.05 m meant that the peak heat-transfer rate calculated by the RANS calculations went up by 26%.

Ten-Degree Sphere-Cone at Mach 7 Zero-Lift Condition

The same baseline geometry was used to spawn five different channeled derivatives with channel radii varying from 0.11 to 0.16 m. For $\alpha = 0$ deg faster axisymmetric flow calculations can be used to understand the effect of variation in channel size. The coarser grids described before were used to create Navier–Stokes flowfield solutions.

Figures 6a–6c depict the variation in flow structure via Mach-number distributions as the channel radius is decreased. With $r_c = 0.16$ m the bow shocks from the lips interact strongly, and flow in the channel is high supersonic. Figure 6b shows that decreasing

Table 1 Comparison of 10-deg sphere-cone performance ($M_\infty = 7.0$, $h = 20$ km, $T_{wall} = 500$ K, $\alpha = 5$ deg)

Geometry	c_l	c_d	$\dot{q}_{max}$, W/m^2
Baseline	0.043	0.512	3.7×10^6
ABLE	0.052	0.493	4.6×10^6

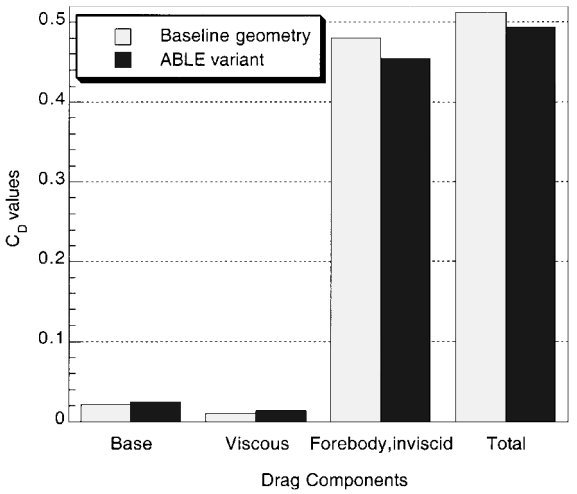

Fig. 5 Comparison of computed drag breakdowns for baseline and ABLE sphere-cones: $M_\infty = 7.0, h = 20$ km, and $\alpha = 5$ deg.

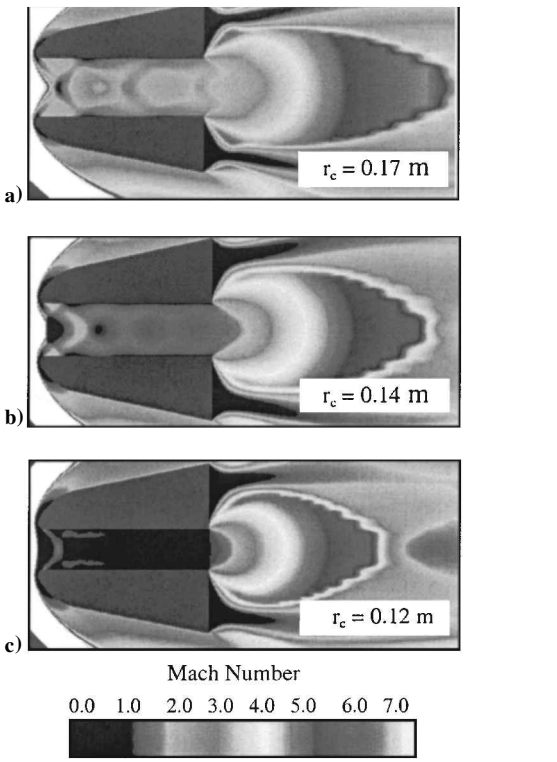

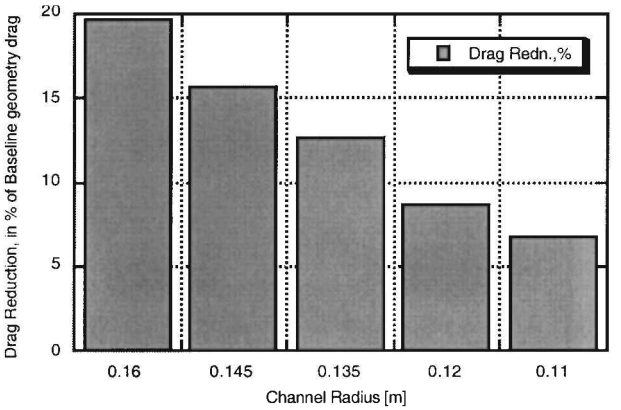

d) Variation of drag reduction with channel size

Fig. 6 Results from axisymmetric Navier–Stokes simulations to measure effect of channel size variation: $M_\infty = 7.0, h = 20$ km, and $\alpha = 0$ deg.

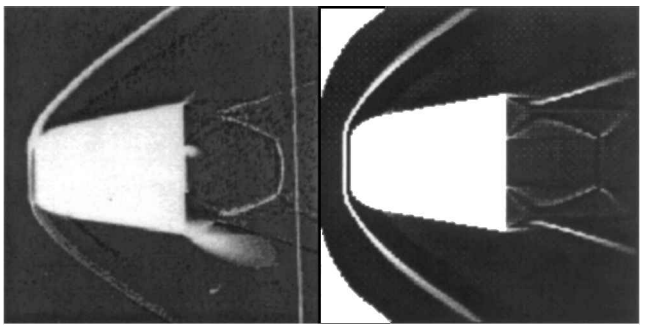

Fig. 7 Comparison of shadowgraph from ABR experiments (left) with simulated shadowgraph derived from RANS calculations (right): $M_\infty = 2.396, h = 0$ km, and $\alpha = 0$ deg.

the r_c to 0.145 m causes the bow shocks to coalesce to a normal shock near the body centerline as the flow in the channel begins to choke. The ABLE configuration, with the fully choked channel, of this set is reached with $r_c = 0.12$ m shown in Fig. 6c. Figure 6d shows the variation in reduction of c_d (based on baseline geometry's base area) with channel size. As expected, a larger channel, which removes more stagnation wall area, provides better drag reduction. All geometries tested had a small $r_{n,l} = 0.035$ m and higher peak heating rates with even the ABLE geometries with $r_c = 0.12$ m, 0.11 m having heating rates around 40% higher than that of the baseline.

Ten-Degree Sphere-Cone at Mach 2–2.5

Similar simulations were conducted for the same baseline sphere-cone geometry scaled to approximately 1:40 at a different flight condition: Mach 2–2.5 at sea level to quantify the benefit in the supersonic regime. With a lower Mach number the channel size can be larger than the nonlifting cases presented in the preceding section and still create the effective blunt-body flow structure. For these cases presented in the next two subsections, a channel radius of 0.175 m is used.

Experimental Verification at $\alpha = 0$ deg

Models of these sphere-cone geometries were also tested at the NASA Ames Research Center Aeroballistic Range (ABR) to provide experimental verification of the computational predictions. Numerous experimental tests of the models were conducted at an average flight Mach Number of 2.25 at sea-level conditions. A comparison of an experimental shadowgraph and a simulated shadowgraph based on a turbulent Navier–Stokes calculation of the model with the channel at Mach 2.396, $\alpha = 0$ deg is shown in Fig. 7. The computed flow structure including the detached bow shock and plume-like flow at the channel exit are validated by the experimental shadowgraph. In addition, the presence and location of the Mach disc in the computed flowfield is verified. Experimental tests of the model with and without the channel indicate that the channel reduces the zero-lift drag at $M = 2.25$ by 9.2% (relative to the baseline value). In comparison, the simulations predicted a drag reduction of about 8.4%. Whereas the c_d for the ABLE sphere-cone was overpredicted by 3.8% from the experimental value, the c_d for the baseline sphere-cone was off by 2.9%. Similar comparisons indicating good agreement between the calculated and the experimental values for drag reduction and c_d at other Mach numbers are presented in Fig. 8. The maximum difference between the calculated and measured c_d values for any geometry was less than 4%. This consistent overprediction of drag is perhaps caused by the use of the efficient but not very precise Baldwin–Lomax model to model the turbulent separated flow in the base regions of the models.

Results at $\alpha \neq 0$ deg

Computations at Mach 2.25, $\alpha = 2$ deg predicted an increase in lift of about 28% caused by the suction region at the lip while the channel reduces total drag by about 7% to give an overall increase in L/D of about 38%. Preliminary analysis of ABR data indicates a

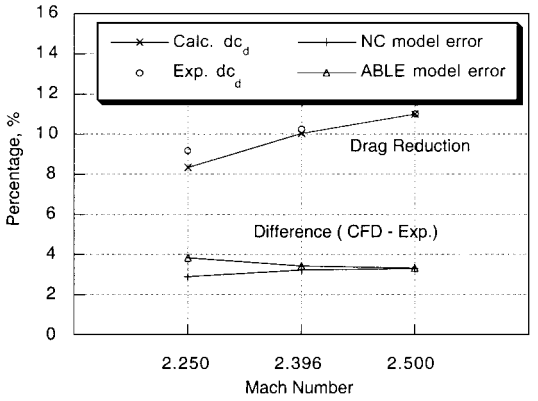

Fig. 8 Comparison of calculated (RANS) and experimental (ABR) results: $\alpha = 0$ deg, sea level.

measured L/D increase of about 32%. More comparisons at lifting conditions have been presented by Gupta.[7] However, a large channel substantially reduces usable volume from the configuration.

Seventeen-and-One-Half-Degree Sphere-Cone at Mach 7 at $\alpha = 0$ Deg

A 17.5-deg sphere-cone with $d_b = 2$ m, $r_n = 0.5$ m, and $r_c = 0.1$ m was tested at freestream conditions of Mach 7 and 16 km altitude to investigate the effect of ABLE on a less slender geometry. There were no significant differences in the flowfield, and a drag reduction of 3.5% for the small channel size was calculated.

When a channel is utilized, the maximum heating occurs at the channel lip, and other studies have been conducted, which indicate that this heating rate decreases as $r_{n,l}$ is increased. However, a larger lip radius is a blunter lip, which will have greater drag. Whereas increasing the channel size leads to a larger wave drag reduction, the increase in wetted area and hence viscous drag has a competing effect on overall drag reduction. To evaluate the practicality of this concept, we need to design a channel (size, lip radius) that will increase aerodynamic efficiency without increasing aerothermal loading. Such a process will have to account for and characterize all of the effects just mentioned over a design space.

Concept Evaluation Methodology

To assess comprehensively the possible benefit of the ABLE concept for sphere-cones, a much larger set of numerical experiments is needed. The analysis just described was only a preliminary evaluation of the efficacy of the channel concept in improving the L/D ratios of sphere-cone bodies with one parameter being varied one at a time. The effect of one parameter on, and in conjunction with, the other must also be accounted for. The flowfield, as demonstrated in the initial analysis, is complex and highly nonlinear such that conceptual/preliminary design level tools cannot characterize it accurately. Also, reduced-order methods create numerical noise[8] that can degrade the reliability of gradient-based optimization procedures by creating local minima. So high-fidelity analyses like RANS simulations are needed to evaluate and optimize different designs. Use of these expensive methods then places a premium on finding the most efficient way of doing so.

An efficient concept evaluation method based on a MDO technique called RSM[9] was formulated and used previously by Gupta and Ruffin for the aerothermodynamic design of an ABLE airfoil.[2] The results of the process are polynomial approximations for desired responses like force coefficients to characterize the design space; these can then be linked to an optimizer to locate the optimal geometry or used as fast analysis replacements for expensive computational fluid dynamics (CFD) analyses. An added advantage is that these models smoothly filter out numerical noise, present even in high-fidelity CFD solutions, to give accurate predictions. The sources of this noise consist mainly of the solution's sensitivity to grid spacing, orthogonality and skewness, discretization errors, and variations in convergence of iterative solutions.

The accuracy of the response surface model and the cost of creating it depends on the choice of experimental design, i.e., an array of point designs chosen mathematically to characterize the effects of and any required interactions between the design variables. Design of Experiments (DoE)[10] is a set of statistical techniques to reduce the full factorial experiment to this required smaller, yet meaningful subset. The use of DoE also avoids biasing the analysis (i.e., being influenced by the level of one design variable), which is typical of a parametric study. DoE, in turn, needs to provide a good fit of the model to the data and so depends on the type of model sought. It also has to give sufficient information to allow for the use of statistical quality measures from regression analysis. These needs usually conflict with cost effectiveness, and thus a compromise between the number of experiments specified and resolution of experimental design is sought. As a result, saturated or near-saturated designs that have run sizes close to the number of terms in the expected model are used.

Second-order models have been typically used in the past to try and capture the non-linearities in system responses. Myers and Montgomery[9] present a detailed description of different experimental designs used for this purpose. The maximization of the D-Optimality criterion,[11] which seeks to minimize generalized variance of the responses as well as parameter estimates, has been a widely used technique[12,13] for experimental design especially when constraints cause an irregular design space. Subsequently, regression analysis is used to characterize the design space, i.e., modeling the responses, of an experiment as functions of the independent variables. The model's accuracy depends on an appreciation of the physical relationships between responses and variables. The functional relationship between a response y and the independent design variables x_i can be expressed as

$$y = F(x_1, x_2, x_3, \ldots, x_k) + \varepsilon \tag{1}$$

where ε represents the total error (i.e., variability not accounted for by F) and k the number of design variables affecting the response. RSM seeks to create an approximation for the unknown function F that can be written as

$$\hat{y} = \beta_0 + \sum_{i=1}^{k} \beta_i x_i + \sum_{i=1}^{k} \sum_{j=1}^{k} \beta_{i,j} x_i x_j \tag{2}$$

where the β are the unknown parameters that need to be estimated. The Least-Squares Method is used to calculate these parameters and create the model. There are several techniques[9,10] to choose the best, or to refine a regression model. The model needs to have an accurate predictive capability, and its coefficients need to be estimated with a good degree of confidence. The t-statistic and F-ratios provide measures to test the significance of each term in the model. The overall quality of the model can be quantified by the R^2, R^2_{adj} and residual error values. The procedure to obtain the final models was described in detail by Gupta and Ruffin.[14] The minimum number of runs required to fit the model in Eq. (2) is given by $0.5(k + 1)(k + 2)$.

Implementation

The candidate geometries were all meant to be designed for operation at Mach 7.0 and 20 km altitude. The baseline and all ABLE sphere-cone geometries have $c = 1.16$ m and $r_n = 0.35$ m. As the objective of the design study is to obtain an ABLE variant from a given sphere-cone shape, the only design variables are those that describe the circular channel shape and size, i.e., r_c and $r_{n,l}$. Table 2 lists the two design variables and their ranges that were discretized. The maximum value of r_c is a function of M_∞ and r_n: this and other geometric relations were used as filters to generate a set of 32 feasible ABLE geometries. A near-saturated D-Optimal design of experiments with nine runs was then obtained by using the JMP[15] Statistical Analysis software. The RANS solutions for each of these geometries were created using the fine grids and high-fidelity solution procedure outlined before. These experiments capture the effect of large lip radii, not investigated so far, in mitigating larger heat-transfer rates.

Table 2 Variables and ranges used to generate the candidate geometries

Variable	Range, m	Levels
r_c	0.05–0.125	6
$r_{n,l}$	0.025–0.11	6

Response equations were created for the force coefficients and maximum heating rates. For the force coefficients, models for Δc_d and Δc_l were created as functions of (r_c/d_b), $(r_{n,l}/d_b)$ while the normalized peak heat-transfer rate was modeled by r_c, $r_{n,l}$. For the Δc_l response surface equation (RSE) a respectable R^2 value of 0.96 was obtained; dropping the intercept term from that RSE decreased the error estimate even further and improved the significance estimates of the effects in the model. Hence the RSE used was in the form

$$\Delta c_l = a_0 r_{n,l} - a_1 r_{n,l} r_c + a_2 r_c^2 \tag{3}$$

The Δc_d RSE had a R^2 value of 0.987 and a small rms error ~0.73. It was of the form

$$\Delta c_d = b_0 - b_1 r_{n,l} + b_2 r_{n,l}^2 + b_3 r_{n,l} r_c - b_4 r_c^2 \tag{4}$$

To capture the dependence of the peak heat-transfer rate of the ABLE geometry accurately, a variable transformation was required: from $r_{n,l}$ to $(r_{n,l})^{-0.5}$. The (cubic) RSE created had a R^2 value of 0.97 and a small rms error of approximately 0.15:

$$q_{\text{norm}} = \dot{q}/10^6 \text{ W/m}^2 = c_0 + c_1 r_c - c_2 (1/r_{n,l})^{\frac{1}{2}} + c_3 (1/r_{n,l}) + c_4 (1/r_{n,l})^{\frac{3}{2}} \tag{5}$$

The coefficients a_i, b_i, and c_i are presented in the Appendix.

Optimization: Results, Verification

The next step was to generate optimal ABLE geometries by coupling the response models with a gradient-based optimizer. Two cases were considered: 1) maximization of L/D for the same external geometry as the baseline sphere-cone and 2) maximization of L/D with the ABLE sphere-cone being scaled up to provide the same internal volume. The maximum allowable heat-transfer rate was constrained to be less than or equal to that of the baseline sphere-cone, 3.7×10^6 W/m^2. Similarly, the force coefficients were constrained to be better than the baseline c_l and c_d of 0.0431 and 0.512 (based on the base area), which provides a baseline L/D value of 0.0842. Thus the overall benefit of an ABLE sphere-cone with an optimal channel geometry that meets the heating load requirements and maximizes L/D enhancement could be determined.

For case 1 the Sequential Quadratic Programming method was used to generate an optimal geometry with a predicted ΔL/D of 4.3%. For case 2 the geometry was scaled up photographically by about 5.4%, and the heat transfer rate constraint drove the design toward the same local lip geometry providing a predicted ΔL/D of 5.15%. Table 3 compares the two optimal geometries. In both cases the optimizer drove the channel radius toward the lower limit; this is unlike earlier behavior for two-dimensional geometry optimization as the drag reduction now has a weaker dependence on the percentage of nose region area removed by the channel and is influenced more by the lip radius. Also, a smaller channel allows for a less constrained lip radius range. The optimal ABLE geometries, shown in Fig. 9, were analyzed via RANS simulations to verify the effectiveness and accuracy of the RSM-based methodology for aerothermodynamic design. A comparison of the predicted force coefficients, L/D ratios, and peak heat-transfer rates with calculated values included in Table 3 shows good agreement for both optimal ABLE sphere-cone geometries. The calculated peak heat-transfer rate for the case 1 geometry was slightly higher than the predicted value by 3.4%. The case 2 geometry, with a larger nose radius, had a lower heat-transfer rate than both the baseline and the unscaled ABLE geometries with the calculated value differing from the predicted value by 0.54%.

Table 3 Comparison of optimal geometries and verification with RANS solutions at $M_\infty = 7.0$, $h = 20$ km, $T_{\text{wall}} = 500$ K, and $\alpha = 5$ deg

Variable	Case 1	Case 2
Length	1.1614 m[a]	1.2242 m
r_n	0.350 m[a]	0.369 m
r_c	0.050 m[a]	0.050 m
r_{base}	0.500 m[a]	0.527 m
$r_{n,l}$	0.063 m	0.063 m
$\Delta(\text{L/D})_{\text{predicted}}$[b]	4.34%	5.15%
$\Delta(\text{L/D})_{\text{calc.,RANS}}$	5.81%	5.57%
Peak $\dot{q}_{\text{calc.,RANS}}$	3.82×10^6 W/m^2	3.68×10^6 W/m^2

[a]Same as baseline. [b]Predicted using RSEs.

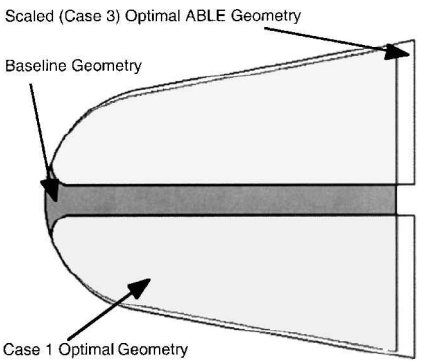

Fig. 9 Comparison of the optimal ABLE sphere-cones with the baseline geometry.

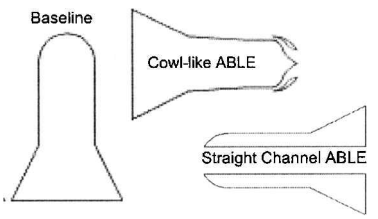

Fig. 10 Baseline blunted configuration with conical flared afterbody (left) and its ABLE variants (right).

Channel Geometry Variations

In most of the numerical studies so far, the internal flow in the straight channel caused an increase in base drag and viscous drag degrading the expected drag reduction. The channel not only compromises the volumetric/packaging efficiency of the configuration but also increases the thermal and structural loads in the interior of the vehicle. These issues need to be addressed by modifying the ABLE geometry so as to preserve the blunted leading-edge effect but shortening the internal flowpath. In one such variation the channel from the leading edge curves out and is exhausted parallel to the body near the shoulder of the body so that a cowl-like geometry is created. Figure 10 depicts the concept applied to a geometry with spherical nose and a conical flared afterbody and compares it with a straight-channel ABLE variant.

Navier–Stokes calculations assuming (axisymmetric) laminar flow at Mach 2.5, $h = 12$ km, and $\alpha = 0$ deg were conducted. The Mach-number distribution for the complex flow presents the interactions between the channel jet and the flow expanding over the shoulder of the sphere-cone in Fig. 11. The channel geometry can be chosen to minimize these interactions and minimize total pressure losses in the internal flow. The flowfield over, and hence the drag contribution of, the spherical nose is similar for both ABLE variants. The drag breakdowns for both ABLE variants are compared to that of the baseline in Fig. 12. The straight-channel ABLE geometry had a total drag 3.9% lower than that of the baseline, and the cowl-like ABLE variant's total drag was reduced further by 5.7% relative to the baseline. Considering only forebody drag, the inviscid drag penalty caused by the flow in the curved channel causes the cowl-like geometry to have a slightly smaller reduction (7% as opposed to 8.4% for the straight channel ABLE). However, the cowl-like geometry does not experience the increase in base drag observed in the straight-channel case. The increase in hot structure as well as viscous drag is smaller because of a smaller increase in wetted surface

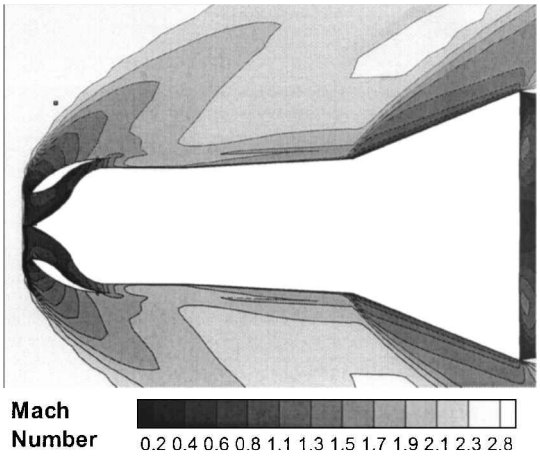

Fig. 11 Mach distribution for the cowl-like ABLE configuration at $M_\infty = 2.5$, $h = 0$ km, and $\alpha = 0$ deg.

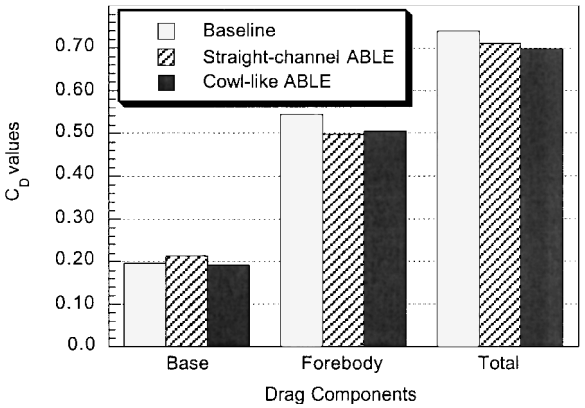

Fig. 12 Calculated drag breakdowns/comparisons for ABLE variants in laminar flow: $M_\infty = 2.5$, $h = 0$ km, and $\alpha = 0$ deg.

area of the cowl-like geometry compared to the straight-channel geometry. The cowl-like shape also has significantly greater usable volume compared to the straight-channel geometry and also reduces potential structural problems.

Conclusions

Initial proof-of-concept Navier–Stokes simulations have validated the ABLE L/D enhancement concept for sphere-cone bodies. This L/D increase was quantified over different flight conditions and geometries. At Mach 7, $h = 20$ km, $\alpha = 5$ deg, L/D increases of about 25% were computed. Computed drag reductions of about 10% at zero-lift, sea-level conditions for Mach 2.25–2.5 show good correlation with experimental data from the NASA Ames Research Center ABR. In lifting flight ($\alpha = 2$ deg), a 10-deg sphere-cone at Mach 2.25 and sea-level conditions can show an improvement in L/D of more than 30%. The ABLE geometry generates significantly higher lift relative to a solid blunt body because of the flow expansion and suction at the channel entrance/lip.

An aerothermodynamic design effort that characterizes the effect of geometry variation on aeroheating loads was undertaken to obtain a channeled sphere-cone geometry that maximizes L/D while ensuring that no penalties are paid in (peak) aerothermal loading. The method uses a RSM to characterize the design space efficiently. The polynomial models developed were used to create optimal ABLE designs that have predicted L/D improvements of approximately 5%. This includes the case where the sphere-cone was scaled up to account for loss of internal volume caused by the channel. The accuracy and effectiveness of the design method was then verified numerically via RANS simulations. As ABLE designs with straight channels can impose several constraints on configuration design, an ABLE variant that exhausts the channel parallel to and near the shoulder of the body was investigated. This variant provided performance enhancement comparable to the straight-channel geometry while minimizing impacts on structural and thermal design as well as on internal packaging. Thus a candidate technique towards a more practical implementation of the ABLE concept than a straight channel was established.

For all of the ABLE sphere-cones, the suction region created at the lip affects not only the lift to provide better L/D but also the c_m and can be used to enhance controllability. A similar effect can be obtained by tailoring the channel exhaust-mean flow interactions. Thus the potential to use the high-pressure underexpanded channel flow for further enhancement of aerothermodynamic performance has been established.

Appendix: Response Surface Coefficients

Response surface equation coefficients are as follows:

$$a_0 = 360.99, \quad b_0 = 4.52, \quad c_0 = 26.93$$
$$a_1 = 9822.63, \quad b_1 = 208.15, \quad c_1 = 8.76$$
$$a_2 = 4705.91, \quad b_2 = 1017.07, \quad c_2 = 18.62$$
$$b_3 = 1994.86, \quad c_3 = 4.58$$
$$b_4 = 1011.9, \quad c_4 = 0.35$$

Acknowledgments

Computational resources provided by L. N. Sankar at Georgia Tech and the Reacting Flow Environments Branch at NASA Ames Research Center are gratefully acknowledged. Support from John Olds at Georgia Tech for the optimization effort is also acknowledged.

References

[1]Ruffin, S. M., Gupta, A., and Marshall, D., "Supersonic Channel Airfoils for Reduced Drag," *AIAA Journal*, Vol. 38, No. 3, 2000, pp. 480–486; also AIAA Paper 97-0517, Jan. 1997.

[2]Gupta, A., and Ruffin, S. R., "Aerothermodynamic Design of Supersonic Channel Airfoils for Drag Reduction," *Journal of Aerospace—SAE 1997 Transactions*, Vol. 106, Sec. 1, 1997, pp. 1647–1656; also AIAA Paper 97-5572, Oct. 1997.

[3]McGrory, W. D., Slack, D. C., Applebaum, M. P., and Walters, R. W., "GASP Version 3, The General Aerodynamic Simulation Program—User's Manual," AeroSoft, Inc., Blacksburg, VA, May 1996.

[4]Steinbrunner, J. P., Chawner, J. P., and Fouts, C. L., "The Gridgen 3D Multiple Block Grid Generation System," Vols. 1 and 2, Wright Research and Development Center, WRDC-TR-90-3022, Wright–Patterson AFB, OH, Feb. 1991.

[5]Palmer, G. E., "High Fidelity Thermal Protection System Sizing of Reusable Launch Vehicle," *Journal of Spacecraft and Rockets*, Vol. 34, No. 5, 1997, pp. 577–583.

[6]Davies, C. B., and Venkatapathy, E., "The Multidimensional Self-Adaptive Grid Code, SAGEv2," NASA TM 110350, April 1995.

[7]Gupta, A., "The Artificially Blunted Leading Edge Concept for Aerothermodynamic Performance Enhancement," Ph.D. Dissertation, School of Aerospace Engineering, Georgia Inst. of Technology, Atlanta, GA, Aug. 1999.

[8]Giunta, A. A., Balabanov, V., Haim, D., Grossman, B., Mason, W. H., Watson, L. T., and Haftka, R. T., "Wing Design for a High Speed Civil Transport Using a Design of Experiments Methodology," AIAA Paper 96-4001, Sept. 1996.

[9]Myers, R. H., and Montgomery, D. C., *Response Surface Methodology: Process and Product Optimization Using Designed Experiments*, Wiley, New York, 1995, pp. 279–373.

[10]Box, G. E. P., Hunter, W. G., and Hunter, J. S., *Statistics for Experimenters: An Introduction to Design, Data Analysis, and Model Building*, Wiley, New York, 1978, pp. 453–535.

[11]St. John, R. C., "D-Optimality for Regression Designs: A Review," *Technometrics*, Vol. 17, No. 1, 1975, pp. 15–23.

[12]Madsen, J., Shyy, W., Haftka, T., and Liu, J., "Response Surface Techniques for Diffuser Shape Optimization," AIAA Paper 97-1801, June 1997.

[13]Balabanov, V., Kaufman, M., Knill, D. L., Haim, D., Golovidov, O., Giunta, A. A., Haftka, R. T., Grossman, B., Mason, W. H., and Watson, L. T., "Dependence of Optimal Structural Weight on Aerodynamic Shape for a High Speed Civil Transport," AIAA Paper 96-4046, Sept. 1996.

[14]Gupta, A., and Ruffin, S., "Optimal Artificially Blunted Leading Edge Airfoils for Enhanced Aerothermodynamic Performance," *Journal of Spacecraft and Rockets*, Vol. 36, No. 4, 1999, pp. 499–506.

[15]JMP Users Guide, Ver. 3.1, SAS Inst., Inc., Cary, NC, 1995.

T. C. Lin
Associate Editor